Examination of the Effectiveness of Far-field Mathematical Absorber Reflection Suppression in a CATR Through Computational Electromagnetic Simulation

S.F. Gregson[1], C.G. Parini[2], A.C. Newell[3], G.E. Hindman[4]
[1] NSI-MI Technologies LLC., Torrance, CA, USA, sgregson@nsi-mi.com
[2] Queen Mary University of London, London, UK, c.g.parini@qmul.ac.uk
[3] NSI-MI Technologies LLC. Torrance, CA, USA, anewell@nsi-mi.com
[4] NSI-MI Technologies LLC. Torrance, CA, USA, ghindman@nsi-mi.com

***Abstract*—For a little over a decade now, a measurement and post-processing technique named Mathematical Absorber Reflection Suppression (MARS) has been used successfully to identify and then suppress range multi-path effects in spherical [1, 2, 3, 4], cylindrical [5, 6, 7] & planar [8, 9] near-field antenna measurement systems and far-field [10] and compact antenna test ranges [11] with a detailed theoretical treatment being presented in [12]. Much of this early work concentrated on verification by empirical testing however some corroboration was obtained with the use of computational electromagnetic simulations that considered far-field [13] and subsequently near-field cases [14]. The recent development of a highly accurate computational electromagnetic simulation tool that permits the simulation of "measured" far-field pattern data as obtained from using a compact antenna test range (CATR) [15] has for the first time permitted the careful verification of the far-field MARS technique for a given AUT and CATR combination. For the first time, this paper presents simulated "measured" far-field pattern data in the presence of a large scatterer and then verifies the successful extraction of the scattering artefacts using standard FF-MARS processing. Results are presented and discussed.**

***Index Terms*— Compact Antenna Test Range, Computational Electromagnetic, Mathematical Absorber Reflection Supression, Measurement Simulation.**

I. INTRODUCTION

Far-field antenna patterns are generally characterised by exhibiting a spatial variation that has a purely angular dependence. In principle, all of these far-field pattern properties can be obtained by placing the test antenna in a perfectly uniform, homogeneous, transverse electric and magnetic (TEM) plane wave field and then rotating the antenna while recording the received amplitude and/or phase. In practice, the simplest direct method is to produce the illuminating plane wave from a small section of a spherical wave-front with very large radius. This can be achieved by placing a low gain source antenna at a very large distance from the antenna under test (AUT) such that the illuminating field incident over the AUT's aperture closely approximates a perfect TEM wave. An alternative strategy is to collimate the field radiated by the source antenna into a pseudo plane wave by placing the source at the focus of a parabolic reflector. The reflection produces an image of the source at infinity thereby creating a TEM plane-wave that can be used to illuminate the test antenna. The popularity of direct collimating antenna range measurements can stem from several factors. These can include: the simplicity with which far-field parameters can be obtained from the experimental equipment, the absence of a requirement to undertake intensive mathematical analysis, the ability to acquire boresight and pattern cut-data very efficiently without the need to first acquire two-dimensional pattern data, the ability to perform real-time measurements using arbitrary waveforms, and the ability to move testing indoors to a highly repeatable, anechoic test environment.

However, no test environment is perfectly adiabatic and it is often found that reflections within antenna test ranges can be the largest source of measurement error within the facility level error budget [16] with direct collimating ranges being perhaps the most susceptible to these contaminants [11, 12]. The recent implementation of an extensive validation campaign for a new CATR computational electromagnetic (CEM) simulation tool that permits the derivation of the error to signal level for a specified AUT and CATR combination [15] admits the possibility of further verification of the FF-MARS technique. Thus, in addition to being able to provide conventional CATR QZ performance metrics such as amplitude taper, amplitude & phase peak-to-peak ripple, it is also possible to provide full-sphere simulated far-field measured data for a given CATR AUT combination including certain measurement errors. The following sections describe the CATR system being modelled presenting simulated CATR QZ performance parameters, before going on to present the results of a simulated CATR measurement of a pyramidal horn in the presence of a strong spurious scattered signal before finally presenting the results of the FF-MARS post-processed data.

II. Overview of the Measurement Simulation

To illustrate the concept, we use the sector-shaped single offset reflector CATR having no edge treatment presented in Figure 1 [17, 12]. This 3 m, 18 panel CATR forms the 8 GHz to 60 GHz CATR facility at Queen Mary University of London's (QMUL) Antenna Measurement Laboratory. The offset parabolic reflector has a 5.4 m focal length and an overall surface accuracy of approximately 80 microns.

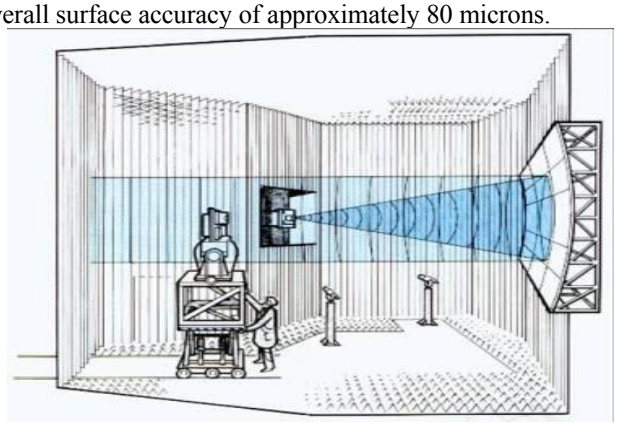

Fig. 1. Schematic representation of sector-shaped single offset reflector CATR at Queen Mary University of London.

In our CEM model the surface profile of the CATR is assumed to be comprised of a perfect concave paraboloidal surface, with the reflector having no edge treatment and being modelled as an ideal metallic knife-edge. Imperfections can be included within the analysis, however, for the present study these are thought to constitute second order effects and so were not included. The phase centre of the range's corrugated horn feed is located at the focus of the offset parabolic reflector with the feed being tilted to an angle of 28° in azimuth so that the edges of the reflector are seen at *circa* ±14° about this direction. At 8 GHz the corrugated feed has an aperture size of 3.39λ and presents an edge illumination in the azimuth plane of approximately -5.0 dB. This particular configuration was chosen as it modelled the CATR that was initially used to verify the FF-MARS technique [11] thereby admitting the possibility of further verification of simulation and measurement. The simulated amplitude and phase of the field illuminating the reflector is shown below in Figure 2 and 3 respectively.

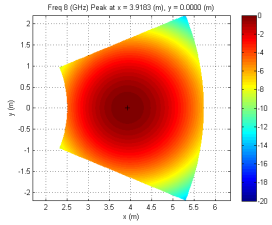

Fig. 2. Magnitude of iluminating fields over sector shaped reflector.

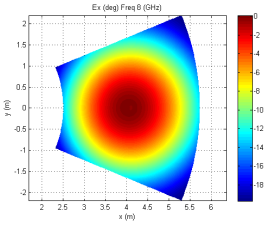

Fig. 3. Phase of *x*-polarised iluminating field over sector shapped reflector.

The current element method [15] replaces the illuminating fields, shown above, with an equivalent surface current density J_s which is used as an equivalent source to the original fields. The surface current density across the surface of the reflector can then be obtained from the incident magnetic fields and the surface unit normal using the physical optics approximation [15, 12]. The field in the CATR quiet-zone (QZ) can then be obtained from the fields radiated by an electric current element which can be obtained from the vector potential and the free-space Green's function [15]. When the field point in the QZ is more than a few wavelengths from the radiating infinitesimal elemental source, the corresponding elemental electric fields can be obtained conveniently from the elemental magnetic fields using the far-field TEM condition with negligible approximation [15]. Thus, both the electric and magnetic fields can be obtained from the elemental fields by integrating over the surface of the reflector. In practice, for the case of a CATR with a QZ located at a distance *z* that is larger than the focal length of the reflector, the error introduced by this approximation is negligible. In this way the fields throughout the volume of space in front of the reflector (*i.e.* outside the deep shadow region) can be computed with great accuracy. To determine the quality of the CATR pseudo plane-wave it is customary for the amplitude and phases to be computed across a plane that is transverse to the range boresight. Figure 4 and 5 below present the amplitude of the principal and cross-polarised electric field for the horizontal and vertical cuts through the centre of the QZ at a frequency of 8 GHz. Here, the transverse plane is located at a distance of 1.136 times the focal length of the reflector from the vertex, *i.e.* 6.13 (m). Here, the best fit 2nd order polynomial which is used to determine the QZ taper is shown plotted in red across a larger 2 x 2m QZ span (the CATR is specified for a 1 m x 1 m QZ).

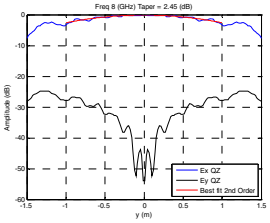

Fig. 4. Principal and cross-polar amplitude across a vertical cut through the CATR QZ, blue trace is *x*-pol field, black trace is *y*-pol field and red trace is least squares quadtratic function denoting amplitude taper.

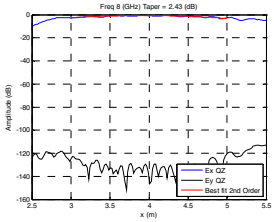

Fig. 5. Principal and cross-polar amplitude across a horizontal cut through the CATR QZ, blue trace is *x*-pol field, blake trace is *y*-pol field and red trace is least squares quadratic function denoting amplitude taper.

It has become customary to specify CATR performance in terms of amplitude taper, and amplitude & phase ripple of this wave throughout a volume of space, termed the quiet zone (QZ). For the QMUL CATR the figures of merit for 1 m x 1 m QZ at a distance z from Vertex to QZ of 6.13 m at 8 GHz the y-axis amplitude taper was 0.63 dB, the y-axis peak to peak amplitude ripple was 1.04 dB and the y-axis peak to peak phase ripple was 5.86°. Conversely the x-axis amplitude taper was 0.63 dB with the x-axis peak to peak amplitude ripple being 1.82 dB and the x-axis peak to peak phase ripple being 10.02°. The slightly worse x-axis results stem from the fact that the offset of the reflector lies within this plane. These values are very close to the industry accepted specifications of

1 dB taper and 1 dB peak-to-peak amplitude ripple and 10° peak-to-peak phase ripple. Unfortunately, in most cases it is not directly apparent how a given QZ performance specification will manifest itself on the resulting far-field antenna pattern measurement and for this reason a sophisticated CEM modelling tool was recently developed that allow "measured" far-field patterns to be produced for a given CATR AUT combination that was based on the reaction theorem which is a well-known method for analyzing coupling problems [15].

This theorem states that, provided the electric *and* magnetic field vectors ($\underline{E}_1$, $\underline{H}_1$) and ($\underline{E}_2$, $\underline{H}_2$) are of the same frequency and monochromatic then the mutual impedance, Z_{21}, between two radiators, antenna 1 (*i.e.* the CATR) and antenna 2 (*i.e.* the AUT), in the environment described by ε, μ can be stated in terms of a closed surface integration. The mutual impedance will clearly be a function of the displacement between the two antennas, their respective orientations, and their relative polarization properties. Once the mutual impedance, and therefore the mutual admittance is known, it is a simple matter to obtain the transmission scattering parameter S_{21} that related the two coupled two-port scattering matrices. The elements $S_{12} = S_{21}$ are the complex transmission coefficients for the coupled antenna system which can be taken to represent a single point within the far-field measurement. This integration can, in principle, be performed across any convenient free-space closed surface however a great deal of computational ease can be sought if a spherical integrating surface is chosen.

Although in principal any closed surface could be used, the advantage of the spherical integration surface is that a general compound rotation can be implemented without the need to compute fields outside this sampling interval. Such isometric vector rotations can be implemented either approximately [12] or rigorously by expanding the fields onto a set of spherical vector mode functions and by rotating those functions [18]. Thus, when utilizing this technique to simulate CATR measurements it is crucial to notice that the fields illuminating the AUT from the CATR only need to be computed *once* per frequency. This is also the case for the fields radiated by the AUT. This makes the processing very efficient with the details of the technique being presented in [15].

For the conventional CATR measurements it is customary for the AUT to be carefully installed within the facility such that the AUT is situated about the axis of rotation. This has the effect of minimizing the volume of the QZ needed and limiting the difference between the direct and indirect (*i.e.* scattered) illumination. However, when taking a MARS type measurement, and entirely contrary to usual antenna measurement practice, we deliberately displace the AUT from the centre of rotation. This has the effect of making the differences between the illuminating field and any scattered field become far more pronounced than would otherwise be the case. And, it is exactly this more significant differentiation that makes their identification and subsequent extraction viable. For the case of a CATR measurement, this has the effect of increasing the size of the QZ that is needed to contain a given AUT than would ordinarily be the case. Thus, for the simulations performed here, the *x*-band SG90 pyramidal horn that was used as the test antenna was simulated located offset from the origin of the measurement co-ordinate system by 0.30 m, 0.61 m and 0.76 m. In each case the electromagnetic six-vector field was computed over the surface of a conceptual sphere with a radius of 0.91 m with a 1° sample spacing in the θ and ϕ axis. The CATR pseudo TEM wave was then computed over a sphere of the same 0.91 m radius that was centered at the point $x = 4.0$ m, $y = 0.0$ m, $z = 6.13$ m. The results of these simulated measurements and the FF-MARS processing can be seen presented in the following section. Note the dimension of the integrating sphere does not need to fit within the QZ of the CATR, instead it is the majority of the current sources that need to remain within the QZ of the CATR for the measurement to be valid. The size and shape of integrating surface is unimportant providing the fields are sampled sufficiently finely across its surface so that the numerical evaluation of the reaction integral is reliable.

III. CATR Simulated FF-MARS Measurements

Experimentally, it has been well established that far-field MARS processing depends upon a measurement that is made with the AUT offset from the origin of the measurement coordinate system combined with a novel mode filtering algorithm [10, 11, 12]. In essence, once the far-field great circle pattern cut has been acquired and the AUT mathematically translated back to the origin of the measurement coordinate system by means of a phase change [12], the equivalent cylindrical mode coefficients (CMCs) can be deduced from far electric fields numerically using standard cylindrical near-field theory incorporating an efficient process that relies upon an inverse fast Fourier transform (FFT). These CMCs can then be filtered to remove artefacts that are not associated with the AUT before the MARS processed far-field pattern can be obtained from the reduced set of CMCs using a FFT based summation procedure.

Figure 6 below contains the CMCs as obtained from a simulated CATR measurement of a WR90 pyramidal horn. Here, the aperture of the horn was located immediately about the origin of the measurement coordinate system. The blue-trace shown in Figure 7 presents the far-field pattern of this ideal measurement and represents the reference pattern, *i.e.* our "truth" model. A large amplitude scatterer was then introduced into the measurement simulation. This comprised a plane wave propagating at 30° in azimuth with respect to the boresight direction of the range with an amplitude that was only 6 dB less than that of the CATR pseudo plane wave. The simulated measurement in the presence of this spurious signal can be seen plotted in Figure 7 as the red-trace. Finally, the black trace represents the FF-MARS processed pattern. Here, the red and black traces are identical (which is why the red trace is not visible in this plot). The absence in offset in this simulated measurement means that the CMCs associated with the AUT and the scatterer are not displaced from one another in the cylindrical mode domain, as is apparent from inspection of Figure 6, and as such the band-pass filter that is applied in

the mode domain does not attenuate the unwanted scattered fields.

However, Figure 9 contains an equivalent simulated measurement only in this case the AUT aperture has been displaced from the origin by 30 cm. When translated back to the origin and transformed to the cylindrical mode domain, as shown in Figure 8, it is clear that there is some degree of separation between the modes associated with the AUT (blue trace) and those associated with the scatterer (red trace). Here, from standard cylindrical near-field theory [12], it is known that the highest order CMC that can be produced by a radiator when situated at the origin of the measurement coordinate system is $N = k_0 a = 18$ where k_0 is the free space propagation constant and a denotes the radius of the minimum cylinder. Thus any higher order mode can be filtered out without affecting the properties of the AUT. Consequently, when filtered and transformed back to the angular domain, there is correspondingly some degree of suppression of the scattered signal as here, in Figure 9, it is clear that the FF-MARS processed pattern (black-trace) is in better agreement with the reference pattern (blue-trace).

However, as the mode spectra are not completely separated the MARS suppression is not complete. Thus, as the AUT is successively translated away from the origin of the measurement coordinate system, as the results in figures 11 and 13 illustrate, the degree of mode separation, (*i.e.* orthogonalisation) also increases as Figures 10 and 12 confirm. Thus, the spurious scattered signal is attenuated more and more effectively. From inspection of Figure 13 it is quite clear that the FF-MARS processing is having a significant effect on the far-field pattern and is very effectively suppressing the effect of the spurious scatterer as the black (FF-MARS processed pattern) is in very close agreement with red (reference) trace. Some small differences are evident in regions of low field intensity, *i.e.* for parts of the pattern that are below, say, – 50 dB.

It is also interesting to note how translating the AUT across progressively larger and larger regions of the CATR QZ also increase the general error level of measurement. The predicted CATR pseudo TEM wave used within these measurement simulations includes amplitude taper stemming from the feed pattern and amplitude and phase ripple primarily emanating from fields diffracting from the knife-edge of the CATR reflector both of which mean that the QZ is of a finite quality and size, *cf.* Figures 4 and 5 above. Thus, as the AUT is progressively offset from the origin the measurement also occupies a larger and larger region of space placing ever greater demands upon the quality of the CATR QZ. This means that although the effectiveness of the FF-MARS processing increases as the AUT offset is increased, other CATR QZ related errors increase eventually compromising the measurement technique. Although not included within these simulations, positioner alignment is also known to become more critical as the magnitude of the AUT offset increase [12]. Thus, although it is preferable to offset the AUT by an amount that is equivalent to the maximum dimension of the AUT, further translation is generally undesirable.

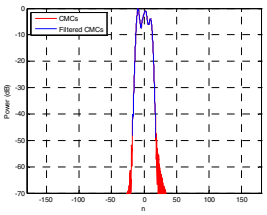

Fig. 6. Cylindrical mode coefficients for 0 m AUT offset case.

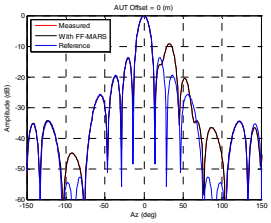

Fig. 7. Far-field amplitude pattern for 0 m AUT offset case.

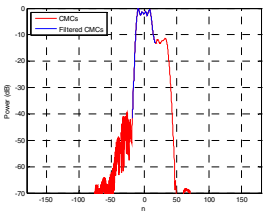

Fig. 8. Cylindrical mode coefficients for 0.30 m AUT offset case.

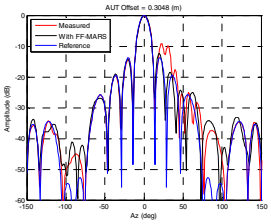

Fig. 9. Far-field amplitude pattern for 0.30 m AUT offset case.

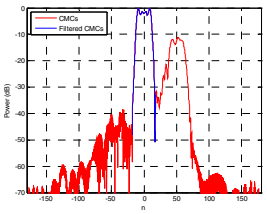

Fig. 10. Cylindrical mode coefficients for 0.61 m AUT offset case.

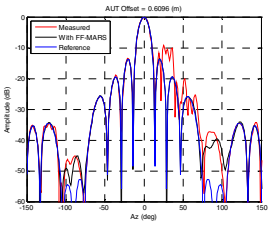

Fig. 11. Far-field amplitude pattern for 0.61 m AUT offset case.

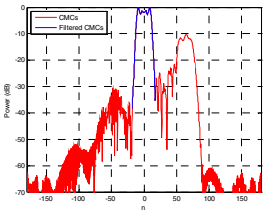

Fig. 12. Cylindrical mode coefficients for 0.76 m AUT offset case.

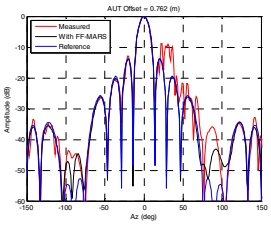

Fig. 13. Far-field amplitude pattern for 0.76 m AUT offset case.

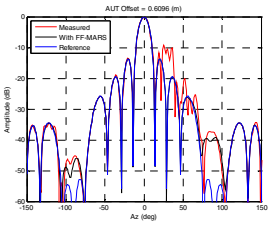

Fig. 14. Far-field amplitude pattern for 0.61 m AUT offset case with cosine squared CMC window function.

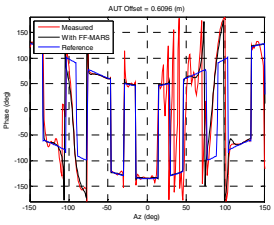

Fig. 15. Far-field phase pattern for 0.61 m AUT offset case with cosine squared CMC window function.

As a final test, the 0.61m AUT offset case was reprocessed using a cosine squared window function. This mode filter imposes less of a discontinuity in the mode domain than the brick-wall band pass filter that is often used and has been seen to provide a minor improvement in the MARS filtered far-field

patterns [13]. From comparison of Figure 14 and figure 11 it can be seen that the degree of agreement attained between the reference pattern and the MARS filtered pattern is marginally improved, especially for the back-lobes. For the sake of completion Figure 14 presents a comparison of the reference and MARS filtered phase plots. Here, it can be seen that the agreement attained is very encouraging everywhere except the region of low amplitude where it is more difficult to control phase, *i.e.* in the null region around ±90°.

IV. Summary And Conclusions

A sophisticated CEM model of a single offset reflector CATR has been used to investigate the impact of various error measurement terms within the facility level error budget of an offset reflector CATR. This model has been used to recreate a conventional FF-MARS measurement whereupon similar phenomena have been observed in the CEM model as have been noted with actual CATR measurements. Specifically these are: 1) the effects of scattering on a far-field pattern depend upon the AUT displacement with larger displacements resulting in higher angular frequency ripple on the far-field patterns, 2) CMCs resulting from scattering are displaced to higher order modes, with AUT modes being displaced to lower order modes once the AUT is mathematically translated back to the origin of the measurement co-ordinate system, 3) the amount of separation between mode distributions associated with scattering and those associated with the AUT increases as the displacement increases, and 4) FF-MARS is capable of effectively suppressing scattering providing the magnitude of the displacement is sufficiently large. This behaviour has also been observed when using spherical mode based expansions, *cf*. [14].

As shown above, the CEM model has been able to provide further confirmation of the effectiveness of the FF-MARS processing showing that it can be used with a very high degree of confidence. All the stages used within the acquisition and post-processing are in common with the well-known and well understood principles of the measurement theory, and all results to date have attested to the success of the method. The AUT displacement and the ensuing finer sample spacing are acceptable providing the sampling criterion is adhered to. The mathematical displacement of origins of the far-field data to the measurement origin is rigorous, with the selection of the mode filter being defined by the physical size of the antenna and its conceptually idealised measurement location. The results of far-field MARS processing will reduce but cannot entirely eliminate the effect of scattering. The final result with MARS processing can be degraded if the translation of the AUT is incorrectly applied, or the mode filter is too tight, i.e. abrupt, but importantly these parameters are controlled by the user.

Finally, as this paper summarises the findings of an on-going programme of research the future plans include investigating the effectiveness of FF-MARS in supressing feed direct illumination of the QZ [14] and the ability of FF-MARS to suppress other non-physical measurement artefacts that stem from imperfections in the CATR pseudo-plane wave.

Acknowledgment

The authors wish to express their thanks to Dr Daniël Janse van Rensburg for his very detailed and constructive review.

References

[1] G.E. Hindman, A.C. Newell, “Spherical Near-Field Self-Comparison Measurements”, AMTA 26th Annual Meeting & Symposium, Atlanta, GA, October 2004.

[2] G.E. Hindman, A.C. Newell, “Reflection Suppression in a large spherical near-field range”, AMTA 27th Annual Meeting & Symposium, Newport, RI, October. 2005.

[3] G.E. Hindman, A.C. Newell, “Reflection Suppression To Improve Anechoic Chamber Performance”, AMTA Europe 2006, Munich, Germany, March 2006.

[4] D.W. Hess, “The IsoFilter™ Technique: Isolating an Individual Radiator from Spherical Near-Field Data Measured in a Contaminated Environment”, EuCAP 2007.

[5] S.F. Gregson, A.C. Newell, G.E. Hindman, “Reflection Suppression in Cylindrical Near-Field Antenna Measurement Systems – Cylindrical MARS”, AMTA 31st Annual Meeting & Symposium, Salt Lake City, UT, November 2009.

[6] S.F. Gregson, A.C. Newell, G.E. Hindman, “Reflection Suppression in Cylindrical Near-Field Measurements of Electrically Small Antennas”, Loughborough Antennas & Propagation Conference, November, 2009.

[7] S.F. Gregson, A.C. Newell, G.E. Hindman, M.J. Carey, “Advances in Cylindrical Mathematical Absorber Reflection Suppression”, 4th European Conference on Antennas and Propagation, Barcelona, 12th - 16th April, 2010.

[8] S.F. Gregson, A.C. Newell, G.E. Hindman, M.J. Carey, "Extension of The Mathematical Absorber Reflection Suppression Technique To The Planar Near-Field Geometry", AMTA, Atlanta, October 2010

[9] S.F. Gregson, A.C. Newell, G.E. Hindman, M.J. Carey, “Application of Mathematical Absorber Reflection Suppression to Planar Near-field Antenna Measurements”, 5th European Conference on Antennas and Propagation, Rome, 11th – 15th April, 2011.

[10] S.F. Gregson, B. Williams, G.F. Masters, A.C. Newell, G.E. Hindman, “Application of Mathematical Absorber Reflection Suppression To Direct Far-Field Antenna Range Measurements”, AMTA, October, 2011.

[11] S.F. Gregson, J. Dupuy, C.G. Parini, A.C. Newell, G.E. Hindman “Application of Mathematical Absorber Reflection Suppression to Far-Field Antenna Measurements”, LAPC November, 2011.

[12] C.G. Parini, S.F. Gregson, J. McCormick, D. Janse van Rensburg “Theory and Practice of Modern Antenna Range Measurements”, IET Press, 2014, ISBN 978-1-84919-560-7.

[13] S.F. Gregson, A.C. Newell, G.E. Hindman, “Examination of Far-Field Mathematical Absorber Reflection Suppression Through Computational Electromagnetic Simulation”, International Journal of Antennas and Propagation, Special Issue on Recent Advances in Near-Field to Far-Field Transformation Techniques, March 2012.

[14] S.F. Gregson, A.C. Newell, G.E. Hindman, “Behaviour of Orthogonal Wave Functions And The Correction of Antenna Measurements Taken in Non-Anechoic Environments”, LAPC, 11-12 November 2013, Loughborough, UK.

[15] C.G. Parini, R. Dubrovka, S.F. Gregson, “CATR Quiet Zone Modelling and the Prediction of “Measured” Radiation Pattern Errors: Comparison using a Variety of Electromagnetic Simulation Methods” AMTA October 2015.

[16] A.C. Newell, “Error Analysis Techniques for Planar Near-field Measurements”, IEEE Transactions on Antennas and Propagation, vol. AP-36, pp. 754-768, June 1988.

[17] A.D. Olver, C.G. Parini, “Millimeterwave Compact Antenna Test Ranges”, JINA November 1992, Nice

[18] J.E. Hansen, “Spherical Near-Field Antenna Measurements”, IEE Electromagnetic Waves Series 26, ISBN 0 86341 110X, 1988.